Draft version February 29, 2024
Typeset using LaTeX default style in AASTeX631

# The dynamic response of Jovian magnetotail reconnection to enhanced solar wind ram pressure

Junjie Chen [1], Binzheng Zhang,[1] Peter A. Delamere,[2] Zhonghua Yao,[1,3] and Oliver Brambles[4]

[1] Department of Earth Sciences, the University of Hong Kong, Pokfulam, Hong Kong SAR, China
[2] Geophysical Institute, University of Alaska Fairbanks, Fairbanks, AK, USA
[3] Key Laboratory of Earth and Planetary Physics, Institute of Geology and Geophysics, Chinese Academy of Sciences, Beijing, China
[4] O.J. Brambles Consulting, Preston, UK

## ABSTRACT

In this study, we employ the Grid Agnostic Magnetohydrodynamic (MHD) for Extended Research Applications (GAMERA), a high-resolving power, three-dimensional global MHD model, to simulate magnetotail reconnection in Jupiter's magnetosphere. While previous satellite observations have provided initial statistics on magnetotail reconnection properties at Jupiter, they have been limited in space-time coverage, leaving the dynamic process of Jovian magnetotail reconnection and its response to the solar wind (SW) poorly understood. Using MHD simulations, we quantitatively analyze the temporal evolution and spatial dependence of nightside reconnection in Jupiter's magnetotail under ideal quiet and enhanced SW conditions. Our results demonstrate that magnetotail reconnection tends to occur in the midnight and post-midnight sectors, with a low occurrence in the pre-midnight sector, consistent with both Galileo and Juno observations and predictions by Delamere & Bagenal (2013). The MLT-radial distribution of magnetotail reconnection is broad, indicating that Jovian magnetotail reconnection is always dynamic rather than steady-state. Enhanced SW ram pressure can decrease the MLT coverage of magnetotail reconnection by compressing Jupiter's magnetosphere. However, the occurrence of magnetotail reconnection near the midnight and post-midnight sectors is enhanced by SW compression beyond $60\ R_J$, but is not significantly impacted by SW compression within $60\ R_J$. Conversely, SW compression suppresses reconnection in the pre-midnight sector, leading to a stronger dawn-dusk asymmetry in the occurrence and location of magnetotail reconnection. This study validates the applicability of the GAMERA code for simulating Jupiter's magnetosphere and provides complementary insights into the dynamic structure and the SW response of Jupiter's magnetosphere.

## 1. INTRODUCTION

Magnetic reconnection is a fundamental process in laboratory and space plasma systems, involving the rearrangement of magnetic topology and energy conversion (Parker 1979; Biskamp 1996; Priest & Forbes 2000; Yamada et al. 2010). This process plays a crucial role in shaping the structure and dynamics of planetary magnetospheres, particularly in the magnetotail region where the magnetic field lines are stretched out by the solar wind (SW). Among all the known magnetotails in the solar system, Jupiter's magnetotail stands out as a unique laboratory for studying space plasma physics due to its unparalleled characteristics such as the largest size, the strongest magnetic field strength, and the fastest rotation.

In contrast to Earth, where the magnetospheric dynamics are primarily determined by magnetic reconnection between the SW/interplanetary magnetic field (IMF) and planetary magnetic field, the dynamics in the Jovian magnetosphere, including its magnetotail region, are mostly driven by planetary rotation due to the large Jovian corotation potential (Khurana et al. 2004; McComas & Bagenal 2007, 2008) and also affected by the viscous-like solar wind interaction (Delamere & Bagenal 2010; Masters 2018). Although there is some debate about the importance of SW reconnection in the Jovian magnetosphere (Cowley et al. 2003, 2008). The unique dynamics of Jovian magnetotail reconnection can exacerbate the loss of the internal plasma, particularly from the Io torus, to the far magnetotail (Kurth et al.

Corresponding author: Binzheng Zhang
binzh@hku.hk

1982; Khurana et al. 2004; Thomas et al. 2004), and may induce distinctive aurora morphology (Waite et al. 1994; Ajello et al. 1998; Waite et al. 2001; Mauk et al. 2002; Szego et al. 2016; Connerney et al. 2017; Gladstone et al. 2017; Gérard et al. 2018; Grodent et al. 2018; Bonfond et al. 2020; Yao et al. 2020; Guo et al. 2021; Yao et al. 2022). Hence, investigating the Jovian magnetotail reconnection provides valuable insights into the complex interplay between magnetic reconnection and the dynamics of planetary magnetospheres, with important implications for our understanding of space weather and auroral processes in the Jovian magnetosphere.

The Vasyliunas cycle is a well-established theoretical model for describing the average state of magnetotail reconnection and plasma circulation at Jupiter (Vasyliunas 1983). In the Jovian nightside magnetotail, the centrifugal force exerted by the co-rotating plasma can elongate the internal quasi-dipole magnetic flux tubes. As a result, the antiparallel directions or components of the stretched magnetic field lines may reconnect near the equatorial plane, resulting in plasmoid ejections down the magnetotail. Based on this theory and an array of observations and simulations, Delamere & Bagenal (2013) put forth an enhanced theoretical prediction for the Vasyliunas cycle. This prediction takes into account the size of the magnetosphere, which is related to strong viscous-like interaction and the momentum transfer rate from the solar wind, and incorporates locations of various structures, including the tail reconnection X-line. Direct observations of reconnection events in the Jovian magnetotail have been made by the Voyager 1 and 2 flybys in 1979 (Nishida 1983), the Galileo spacecraft from late 1995 to 2003 (Russell et al. 1998; Woch et al. 2002; Kronberg et al. 2005; Vogt et al. 2010) and the Juno spacecraft from July 2016 to present (Vogt et al. 2020), providing important statistics of reconnection event properties such as their spatial extent, recurrence time, and location. Plasma measurements in Jupiter's magnetotail for $\sim 2000\ R_J$ downstream were also provided by the recent flyby of Jupiter by the New Horizons spacecraft (McComas & Bagenal 2007; McNutt et al. 2007), although without magnetometer data, the periodicities in the energetic particle dispersive events suggest plasmoid release from magnetotail reconnection (Hill et al. 2009). Some observational studies have suggested that Jupiter's magnetotail may respond to solar wind ram pressure, with most relying on model predictions or indirect Ulysses data as substitutes for upstream solar wind data (Tao et al. 2005; Ge et al. 2007; Vogt et al. 2019), except for one dual spacecraft observation event but without reconnection signature (Hanlon et al. 2004). However, due to insufficient data coverage of observations and the inseparability of space-time information in single-spacecraft measurements, the dynamic structure of magnetotail reconnection and its response to the SW have not been well understood. In addition, previous studies using magnetohydrodynamic (MHD) codes have simulated the magnetotail structures at Jupiter (Ogino et al. 1998; Miyoshi & Kusano 2001; Song et al. 2001; Fukazawa et al. 2006; Moriguchi et al. 2008; Chané et al. 2013; Wang et al. 2018; Sarkango et al. 2019; Tanaka et al. 2021), and some have studied the effect of SW ram pressure on the Jovian magnetotail (Fukazawa et al. 2006; Sarkango et al. 2019; Tanaka et al. 2021), but lacked quantitative comparison of magnetotail reconnection with Galileo/Juno observations and the prediction by Delamere & Bagenal (2013).

The recent development of the Grid Agnostic MHD for Extended Research Applications (GAMERA), a high-resolving power, three-dimensional global MHD code (Lyon et al. 2004; Zhang et al. 2019), has enabled the study of SW-Jupiter interactions with mesoscale-resolving capabilities (Zhang et al. 2018, 2021; Feng et al. 2022; Chen et al. 2023). In this study, we use the GAMERA code to simulate the dynamic structure of Jupiter's magnetotail and its response to the SW ram pressure. First, we show the effectiveness of the MHD model on the Jovian magnetospheric problems by comparing the simulated radial density profile within Jupiter's magnetodisc with observations. Then, we quantitatively analyze the temporal evolution and spatial dependence of nightside reconnection in Jupiter's magnetotail. Furthermore, the response of the Jovian magnetotail reconnection to SW compression is investigated by comparing the magnetotail structures under ideal quiet and enhanced SW conditions.

## 2. METHODS

### 2.1. *The global MHD model*

For simulating the space environment of Jupiter's magnetosphere, the GAMERA code uses a finite-volume technique to solve the ideal MHD equations on a non-orthogonal, curvilinear grid that is adapted to the Jovian magnetospheric problems. The computational grids are based on non-orthogonal stretched spherical grids with 256×256×128 cells corresponding approximately to the spherical (radial×meridional×azimuthal) coordinate. The grids are oriented in solar-magnetospheric coordinates, where the X, Y, and Z axes correspond to the Sun, east (dusk), and north, respectively. The grid resolution varies with radial distance to the planetary center, with the highest radial resolution of 0.1 Jovian Radii ($R_J$) near the inner boundary, which is located at a Jovi-centric distance of 3.5 $R_J$, and with $0.5 \sim 1.5$ $R_J$ resolutions between 37.5–124.2 $R_J$, where most Jovian magnetotail reconnection events were observed (Vogt et al.

2010, 2020). The Jovian magnetospheric simulation extends to 100 $R_J$ in the sunward direction, -1000 $R_J$ in the anti-sunward direction, and ±300 $R_J$ in directions perpendicular to the Sun-Jupiter axis. To simplify the analysis by removing hemispheric asymmetries induced by the tilt, the dipole tilt angle of the Jovian magnetosphere is set to 0. The 10-hour corotation of the Jovian magnetosphere is implemented by imposing a time-stationary corotation potential onto the ionospheric potential (Zhang et al. 2018). The simulated heavy-ion massing loading from the Io plasma torus is 1000 kg/s, added in a ring centered at 6 $R_J$ in the equatorial plane. The ionospheric Pedersen conductance is set to be constant of 0.5 S. The calculation time step varies around 0.2 s, determined by the Courant-Friedrichs-Levy condition (Zhang et al. 2019), and the output time step for statistical analysis is 600 s.

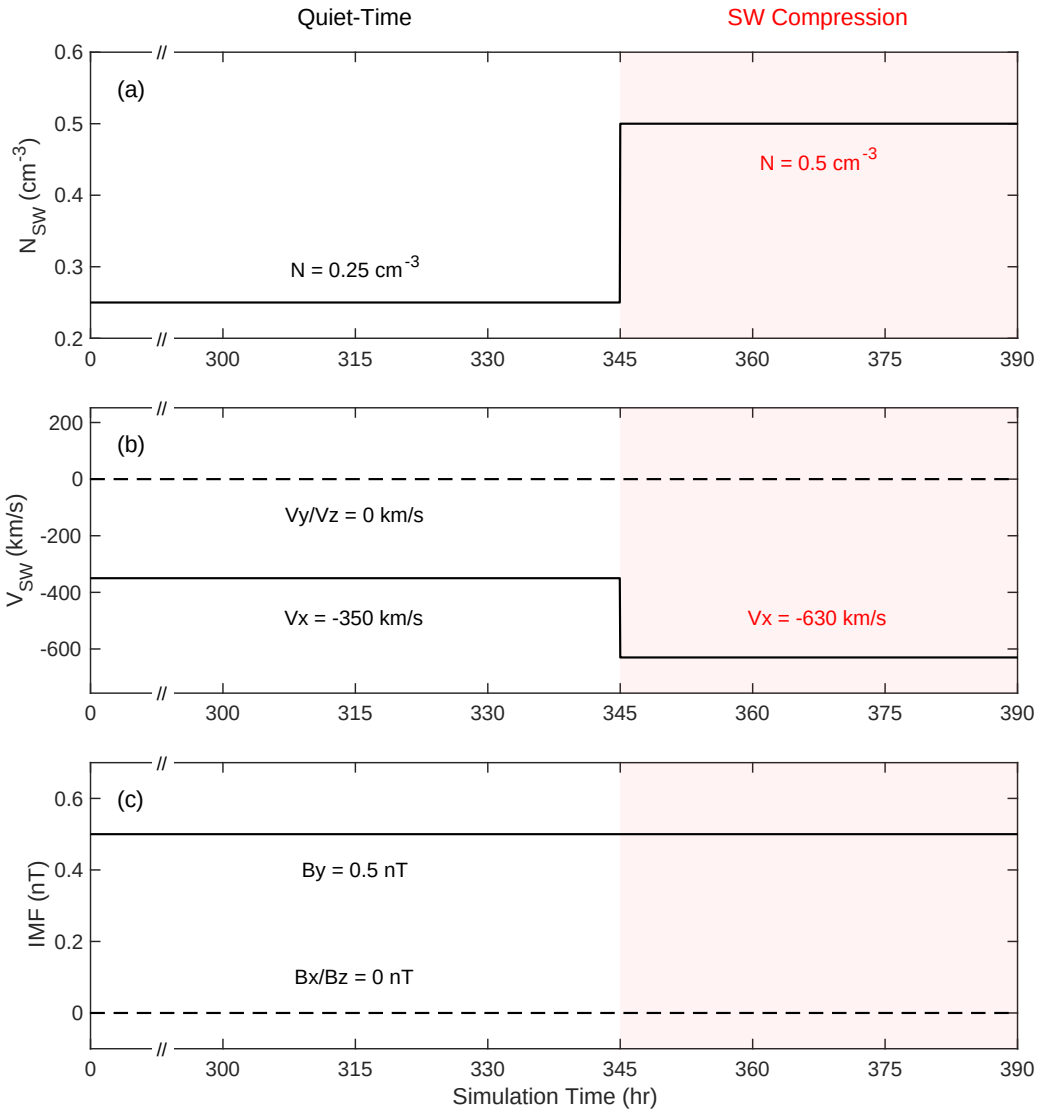


**Figure 1.** The upstream solar wind (SW)/ interplanetary magnetic field (IMF) conditions as used in the simulation. Shown from top to bottom are (a) SW density, (b) SW velocity, and (c) IMF.

Figure 1 depicts the upstream SW/ IMF conditions that drive the global MHD model of Jupiter's magnetosphere. During the initial 0–345 hrs simulation time (ST), the upstream SW temperature, density, velocity, and IMF By are set to quiet-time parameters of $2.0 \times 10^4$ $K$, 0.25 $cm^{-3}$, 350 $km/s$, and 0.5 $nT$, respectively, corresponding to ram pressure of 0.025 $nPa$ and Alfvén Mach numbers of 16.0, based on typical SW/IMF conditions (Blanc et al. 2005; Delamere & Bagenal 2010; Jackman & Arridge 2011). It should be noted that this study analyzes only the simulation data after the

start-up transit ($\sim 300\ hr$) when the average radial profile of the heavy ion density was settled into a quasi-steady state in a spin-averaged sense. To analyze the response of magnetotail reconnection after an SW compression, SW density and velocity are set to enhanced parameters of 0.5 $cm^{-3}$ and 630 $km/s$ during 345 : 00–390 : 00 ST, corresponding to ram pressure of 0.17 $nPa$ and Alfvén Mach numbers of 40.8. The enhanced ram pressure matches the observed Ulysses data (Tao et al. 2005). For convenience, 300:00–345:00 ST is referred to as the quiet-time period, and 345:00–390:00 ST is called the SW compression period.

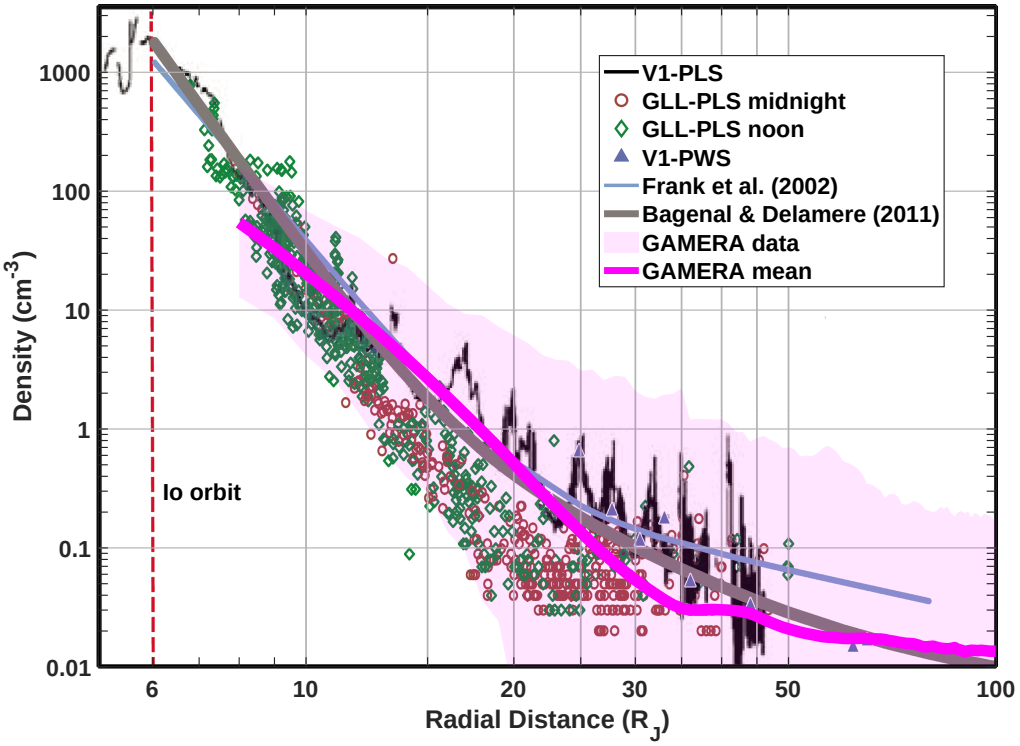


**Figure 2.** Radial density profile in the simulation, compared with Figure 1 from Bagenal & Delamere (2011). The magenta shadow represents the simulated equatorial density data averaged over 300:00–390:00 ST, while the magenta line represents the azimuthal-mean density. Density measurements derived from Voyager 1 PLS (black line), Voyager 1 PWS (blue triangles), and Galileo PLS (all orbits) obtained ±30° around noon (green diamonds) and ±30° around midnight (red circles). The profile from Frank et al. (2002) (pale blue curve) is based on Galileo PLS data from the G8 orbit data obtained on the nightside. The profile from Bagenal & Delamere (2011) (thick gray curve) is a composite of three power law profiles (blue, purple, and yellow lines).

Figure 2 compares the radial density profile within Jupiter's magnetodisc in the MHD simulation with observations to evaluate the effectiveness of the simulation in addressing Jovian magnetospheric issues. Within the range of 10–100 $R_J$, which encompasses the majority of observed Jovian magnetotail reconnection events in the range of 37.5–124.2 $R_J$ (Vogt et al. 2010, 2020), our simulated density profiles exhibit an excellent agreement with in situ measurements and empirical distributions summarized by Bagenal & Delamere (2011). Furthermore, the simulated density displays significant relative variations, as shown in the magenta shadow in Figure 2. Schok et al. (2023) found the relative density variations in the GAMERA simulation between 10–60 $R_J$ were in agreement with the Juno observations between 30–50 $R_J$ (Huscher et al. 2021). These observation-simulation agreements validate that the MHD model is a suitable tool for investigating the dynamic evolution of the Jovian magnetosphere, including the magnetotail reconnection process.

Note that magnetic reconnection in the MHD simulation is enabled by numerical resistivity, i.e., when opposing magnetic flux enters a single computational cell and is then averaged out of existence (Brambles et al. 2011). The rate of reconnection is determined only by the conditions external to the actual reconnection region through the conservation of mass, momentum, and magnetic flux (Lyon et al. 2004; Zhang et al. 2016, 2017). In the simulation

of the terrestrial magnetosphere, Ouellette et al. (2013) have shown that when reconnection is induced by convergent flow, the nightside reconnection rate in the simulation is constrained by a Petschek-like inflow condition to be a fraction ($\approx 0.1$) of the Alfven speed in the inflow, regardless of the grid size. Thus we expect that the global MHD simulation is capable of reproducing large-scale configuration of Jovian magnetotail reconnection, although micro-physics has not been implemented into the Jovian magnetosphere simulation.

### 2.2. *Locating the $B_z$ reversal positions*

In a planetary magnetosphere without dipole tilt and significant hemispheric asymmetry, magnetotail reconnection at the equatorial plane can be identified in the magnetic field by tracking changes in the north-south component of the magnetic field ($B_z$), such as field dipolarizations or $B_z$ reversals (Vogt et al. 2010). In this study, we used a similar method as suggested by Vogt et al. (2010) to find the positions of magnetotail reconnection, but applied it to the high-resolution simulation data. Specifically, we sliced the data at the equatorial plane ($Z = 0$) at evenly 600-second spaced steps during 300:00–390:00 ST and identified positions where $B_z$ reversed from southward (parallel to the background field) to northward (antiparallel) as radial distance increases for each azimuthal index on the nightside ($X < 0$). Figure 9 in APPENDIX provides an example of $B_z$ reversal positions at 300:00 ST. It is important to note that the identified $B_z$ reversal positions may not necessarily correspond to the actual locations where reconnection first occurs when there are radial outflow transports in the magnetotail (Movie S1); however, this method allows for a useful comparison between simulations and observations.

## 3. RESULTS AND DISCUSSION

### 3.1. *Global configuration of Jovian magnetotail reconnection*

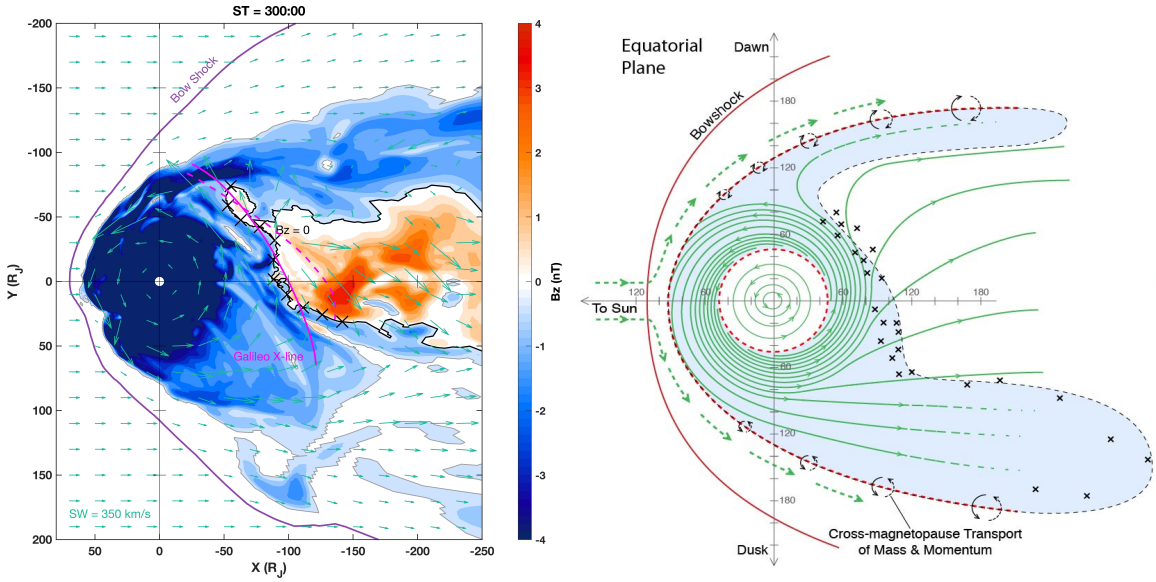


**Figure 3.** (left) The simulated distribution of $B_z$ (positive northward) and plasma flow at the equatorial plane of Jupiter's magnetosphere at 300:00 ST. Black/gray lines indicate the $B_z$ zero lines, "X" patterns mark approximate locations of the X-line, and green arrows represent plasma flows. Additionally, a magenta solid line represents the average location of the X-line based on Galileo magnetic field data from Vogt et al. (2010), and a magenta dashed line denotes the average location of the X-line based on Galileo particle flow data from Woch et al. (2002), excluding the premidnight results with large uncertainty. (right) A schematic of theoretical prediction of the equatorial meridians for the Vasyliunas cycle, adapted from Delamere & Bagenal (2013), showing the average plasma flow (green), the predicted locations of the X-line ("X" pattern), and the regions of closed magnetic flux (light blue). The wings of closed flux on the dawn and dusk flanks are taken from global MHD simulations (Song et al. 2001; Jia et al. 2012) and based on New Horizons dispersive events (McNutt et al. 2007; Hill et al. 2009).

Figure 3 depicts (left) an instantaneous distribution of the simulated $B_z$ and plasma flow in the equatorial plane of the Jovian magnetosphere, compared with the Galileo-observed X-lines based on $B_z$ (magenta solid lines) and plasma flow data (magenta dashed line) and (right) a theoretical prediction for the Vasyliunas cycle in Delamere & Bagenal

(2013). Besides $B_z$ reversals, magnetotail reconnection may also be identified by the reversals of the disturbances in the radial and azimuthal components of the particle flow (Woch et al. 2002). As shown in the left panel of Figure 3, the two Galileo-observed X-lines from $B_z$ (magenta solid line) and plasma flow data (magenta) generally correspond with each other. In the following we mainly compare the MHD results with the Galileo $B_z$ X-line. Within approximately Jovi-centric 100 $R_J$ of the simulated Jovian magnetotail near the midnight meridian, where $B_z$ is parallel with the southward component of internal planetary dipole fields, and magnetospheric plasma corotates in the counterclockwise direction when viewed above the North Pole. Near the midnight meridian outside Jovi-centric 100 $R_J$, $B_z$ has significant south-to-north reversals with the order of 1–4 $nT$ in a cavity (red ranges enclosed by the black line), where plasma flows are generally radially outward and have clockwise azimuthal components. The coverage of the $B_z$-reversed cavity shows a dawn-dusk asymmetry that is wider on the dawnside than on the duskside. Beyond the $B_z$-reversed cavity, there are wing structures of southward $B_z$ on the dawn flank and of disturbed $B_z$ on the dusk flank. The simulated large-scale structure of corotation ranges, $B_z$-reversed cavity and $B_z$-southward/disturbed wings in Jupiter's internal magnetotail is generally consistent with the theoretical picture (the right panel of Figure 3). Specifically, the "X" patterns in the left panel of Figure 3 represent approximate locations of magnetotail reconnection in the simulation, which are located at the "inner" side of the magnetotail $B_z$-zero line. The simulated X-line has a radial distribution similar to those predicted by Delamere & Bagenal (2013) ("X" patterns in the right panel) and observed by the Galileo satellite (magenta line in the left panel). However, the MHD simulation and the theoretical prediction in Figure 3 differ in terms of the magnetospheric size and duskside wings. This difference is a consequence of the fact that the MHD result shown in Figure 3 is just an instantaneous snapshot of the highly dynamic Jovian magnetosphere under ideal SW conditions as shown in Movie S1, whereas the theoretical prediction is based on an average of the statistical data with changing real SW conditions.

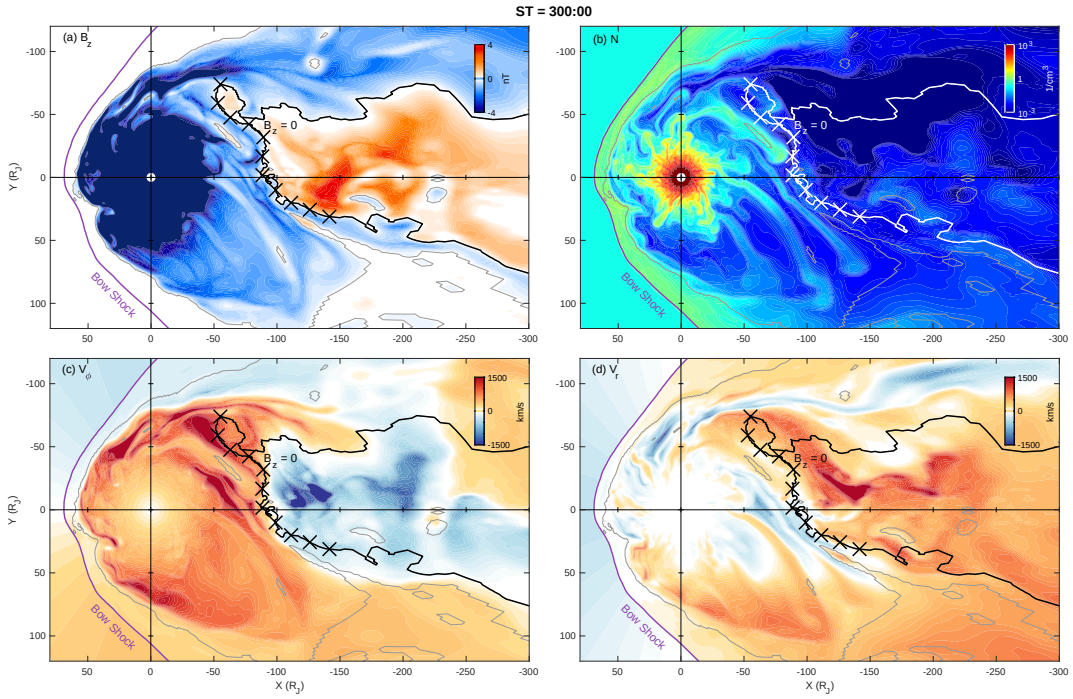


**Figure 4.** The distribution of (a) $B_z$ (positive northward), (b) plasma number density (N), (c) azimuthal flow ($V_\phi$, positive anticlockwise), and (d) radial flow ($V_r$, positive outflow) at the equatorial plane of Jupiter's magnetosphere at 300:00 ST from the MHD simulation. The same snapshot is shown in Figure 3. The contours of $B_z = 0$ are represented by black/white and gray lines in each panel, "X" patterns denote the approximate locations of the X-line. The corresponding animations during 300:00-390:00 ST are available. The video duration is 14 $s$.

To further understand the magnetotail reconnection process, Figure 4 presents distributions of $B_z$, plasma number density, azimuthal and radial flow speeds derived from the same snapshot (300:00 ST) as in the left panel of Figure 3.

Figures 4a–4b show a dense disc-like structure of magnetic field and plasma density within Jovi-centric 30 $R_J$, referred to as the magnetodisc (Delamere et al. 2015; Huscher et al. 2021). Notably, the magnetodisc displays periodic finger-like density-enhanced structures between Jovi-centric 6–40 $R_J$ that corotate with Jupiter and extend outward (see the plasma velocity in Figures 4c–4d). These periodic structures are believed to be generated by the centrifugal force arising from planetary rotation, which was also seen in drift-kinetic simulations of the Jovian magnetosphere (Yang et al. 2019; Wang et al. 2023). Near the magnetotail reconnection locations (marked by "X" patterns), enhancements in clockwise/Jupiter-ward flows and in anticlockwise/tailward flows are evident (Figures 4c–4d). The consistency of the enhancements in radial and azimuthal flows is also observed in the observation (Woch et al. 2002). These enhanced flow speeds are signatures of reconnection exhaust flows due to magnetotail reconnection. The anticlockwise/outward flows generated by magnetotail reconnection can transport the plasma mass and magnetic flux to distant magnetotail, which is known as the plasmoid release process (Kronberg et al. 2005; Vogt et al. 2014). The dynamics of this process are visualized in Movie S1.

### 3.2. *Statistical analysis of the magnetotail reconnection*

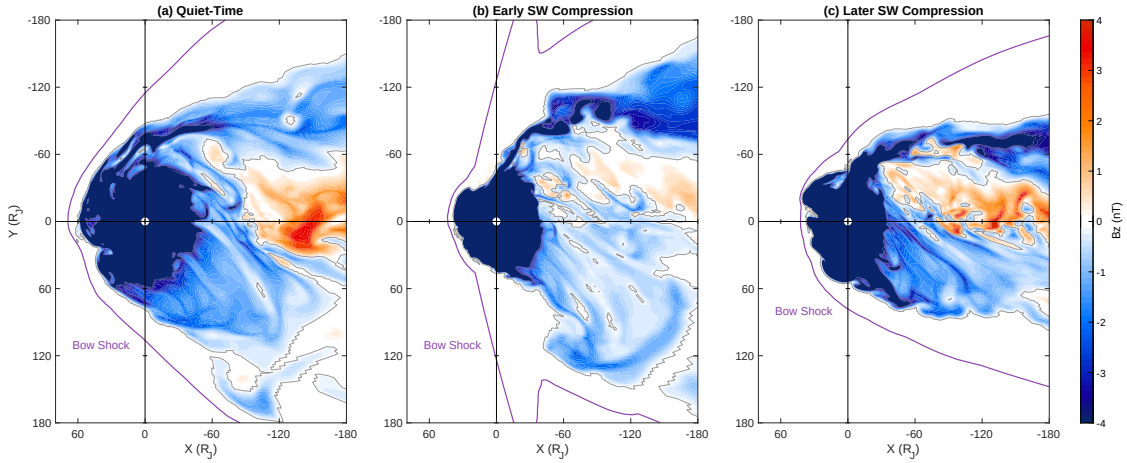


**Figure 5.** Snapshots of equatorial $B_z$ distributions at 300:00, 350:00, and 390:00 ST, which are during the quiet time, the early stages of SW compression, and the later stages of SW compression, respectively.

Figure 5 and Movie S1 reveal that the magnetosphere of Jupiter exhibits three distinct phases over 300:00–390:00 ST. The first phase occurs during the period of quiet-time SW between 300:00 and 345:00 ST. During this phase, the magnetosphere maintains a relatively stable size of approximately 60–70 $R_J$ on the dayside but undergoes hourly periodic dynamic variations. These dynamic variations, which are thought to be associated with the internal activity of Jupiter's highly structured plasmadisc, have been observed by Galileo and Juno (Gu et al. 2023; Schok et al. 2023) and also discussed in detail in the simulation study using the GAMERA model (Feng et al. 2023). The second phase occurs during the early stages of SW compression between 345:00 and 360:00 ST, during which the magnetosphere is rapidly compressed and the dayside scale is reduced from 60 $\sim$ 70 $R_J$ to 40 $\sim$ 45 $R_J$. This transient phase is characterized by highly unstable energy and mass release processes in the magnetotail. The third phase occurs during the later stages of SW compression between 360:00–390:00 ST, in which the magnetosphere remains compressed to a relatively stable scale of 40–45 $R_J$ on the dayside. In this subsection, we focused primarily on the first and third phases, during which Jupiter's magnetosphere exhibited a relatively quasi-steady state rather than a transient state. The second phase will be mentioned in the discussion.

The highly dynamic evolution of the Jovian magnetotail reconnection process exhibits a broad radial-MLT coverage in the equatorial plane (Movie S1). To analyze the statistical distribution of magnetotail reconnection, we performed a statistical analysis of the occurrence rate of $B_z$-reversal cases following a similar method used in Figure 9 of Vogt et al. (2010). This statistical distribution of the magnetotail reconnection is based on radial distance and MLT during quiet-time periods (300:00–345:00 ST) and the later phase of SW compression periods (360:00–390:00 ST). Initially, we segregated the equatorial $B_z$ data from the MHD simulation into bins with a radial distance of 5 $R_J$ and a 0.5-hr interval in MLT. Within each bin, if at least one grid showed a $B_z$ reversal, we identified that bin as a $B_z$ reversal

case and incremented the count by one. The occurrence rate was computed as the number of steps with $B_z$ reversal cases in each bin divided by the total steps during the considered period, given that the output time step was 600 $s$.

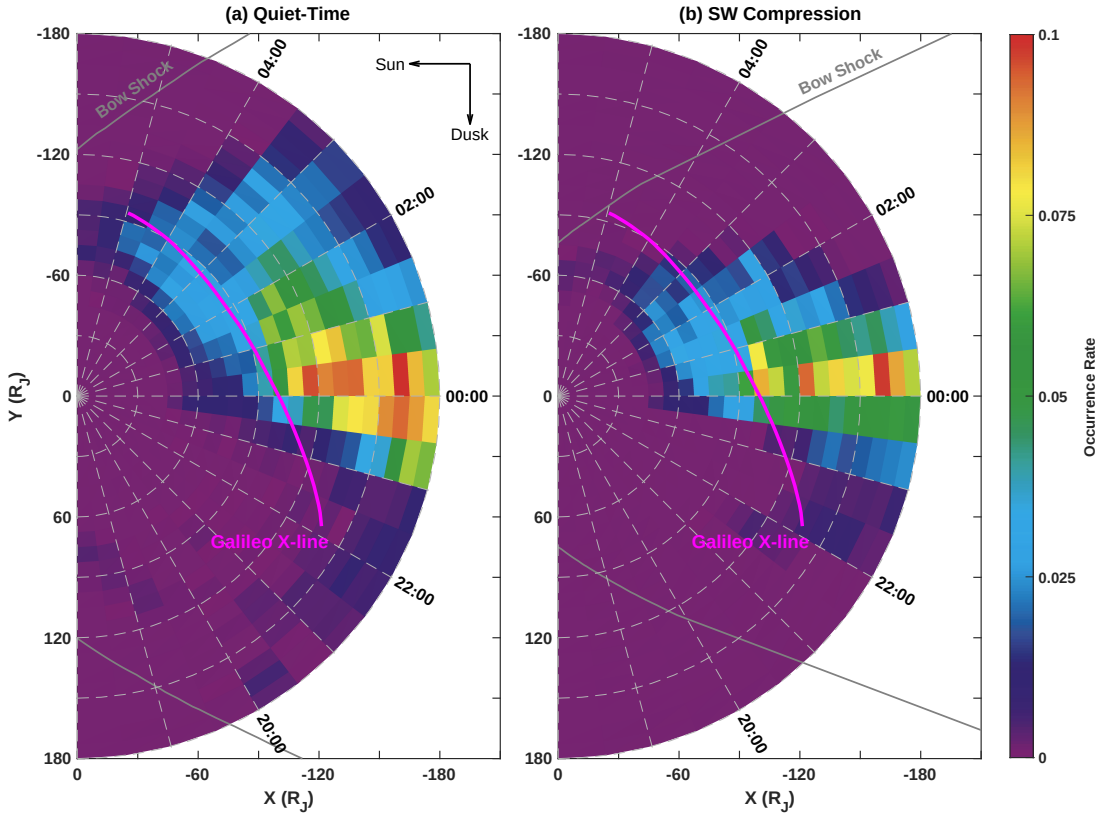


**Figure 6.** The occurrence rate of Bz reversal cases in the MHD simulation for bins of 5 $R_J$ in the radial distance and 0.5 hr in MLT during (a) quiet-time periods between 300:00–345:00 ST, and (b) the later phase of SW compression between 360:00–390:00 ST. The occurrence rate is computed as the event counts with $B_z$ reversal cases in each bin divided by the total data (grid numbers × total time steps), given that the output time step is 600 $s$. The magenta lines represent the average location of the X-line based on Galileo data, adapted from (Vogt et al. 2010)

Figure 6 illustrates the spatial dependence in the occurrence of the $B_z$ reversal cases during quiet-time periods and the later phase of SW compression periods. For both SW conditions, the simulated $B_z$ reversal events are mostly outside Jovi-centric 35 $R_J$, which is consistent with the fact that $B_z$ reversal events were observed by Galileo between 44.09–124.2 $R_J$ (Vogt et al. 2010) and Juno between 37.5–112.7 $R_J$ (Vogt et al. 2020). Most $B_z$ reversal cases occur near the midnight meridian around 0:00 MLT. The occurrence rate of $B_z$ reversal cases in the post-midnight sector (0:00–6:00 MLT) is much higher than that in the pre-midnight sector (18:00–24:00 MLT). This dawn-dusk asymmetry is also seen in the Galileo data that has coverage on both dawnside and duskside for $B_z$ (Vogt et al. 2010) and plasma flow (Woch et al. 2002; Kasahara et al. 2013). As MLT changes from 0:00 to 5:00, the radial position with the maximum occurrence rate decreases from $\sim$ 120 $R_J$ to $\sim$ 80 $R_J$ under SW quiet conditions (Figure 6a), and it decreases from $\sim$ 110 $R_J$ to $\sim$ 70 $R_J$ during SW compression (Figure 6b). This radial distance-MLT relationship is generally consistent with the average location of the Galileo-observed X-line (magenta line).

In comparison to the quiet-time condition shown in Figure 6a, the enhanced SW ram pressure results in a higher occurrence of reconnection beyond 60 $R_J$ and a slight concentration of magnetotail reconnection slightly near the midnight sector, as illustrated in Figure 6b. This could be a result of the impact of SW compression on the equatorial current sheets of giant planets (Smith et al. 1978; Jackman et al. 2010). Meanwhile, as magnetic reconnection occurs

more frequently at positions closer to Jupiter, which may correspond to greater magnetic energy and a stronger reconnection energy flux, ultimately resulting in the observed dawn storm auroras during SW compression periods (Nichols et al. 2007, 2019; Yao et al. 2022). However, the changing of the SW ram pressure has a limited impact on magnetotail reconnection during post-midnight within 60 $R_J$, indicating that the generation of Jovian magnetotail reconnection is mostly driven by the planetary corotation rather than SW effects. In addition, Figure 6 implies that the SW compression can suppress the reconnection on the duskside (18:00–21:00 MLT), which induces a stronger dawn-dusk asymmetry of the magnetotail reconnection. This may be attributed to the smaller volume in the 18:00–21:00 MLT sector in the SW-compressed magnetosphere, which does not support the centrifugal force to generate sufficient magnetic field line stretching to enable magnetotail reconnection.

To further analyze the distribution of magnetotail reconnection, we statistically analyze the distribution of the dominant $B_\theta$ signature, based on a similar method used in Figures 10–11 of Vogt et al. (2010). Here, $B_\theta$ represents the meridional component of magnetic fields, which is positive southward at the equatorial plane, i.e., parallel with Jupiter's dipole magnetic field and opposite to the $B_z$ definition. Based on the common $B_\theta$ directions during a long-term period, each grid point at the equatorial planes was then assigned one of three $B_\theta$ signatures, defined as:

1) $B_\theta$ positive dominated signatures: $B_\theta$ is positive for more than 85% of the duration, which is a similar definition in Vogt et al. (2010).

2) $B_\theta$ negative dominated signatures: $B_\theta$ is negative for more than 50% of the duration. We do not use the same threshold of 85% in Vogt et al. (2010), since few signatures qualify the 85% threshold due to the significant dynamic evolution in the magnetotail (as shown in Movie S1).

3) $B_\theta$ bipolar signatures: the rest of situations that are neither $B_\theta$ positive nor negative dominated signatures.

Figure 7 illustrates the distribution of the dominant $B_\theta$ signature and the location of an inferred X-line during (a) periods of SW quiet time and (b) the later phase of SW compression. Under SW quiet-time conditions (Figure 7a), the equatorial regions are mostly colored red across most MLTs and within Jovi-centric 60 $R_J$, indicating positive $B_\theta$ signatures or inferred inward flows dominate. Between 21:00 and 5:30 MLT, the inner magnetotail experiences bipolar $B_\theta$ dominance (green). It should be noted that the green ranges near the outer boundary of the magnetosphere, which is just a numerical consequence of the dynamic variation in the size of the magnetosphere. The boundary between $B_\theta$ positive and bipolar ranges near the inner magnetotail increases from $\sim$ 60 $R_J$ to $\sim$ 120 $R_J$ with MLT shifting from 5:30 to 21:00, while the boundary between $B_\theta$ bipolar and negative ranges near the inner magnetotail increases from $\sim$ 100 $R_J$ to $\sim$ 180 $R_J$ with MLT shifting from 2:00 to 23:30. Moreover, the average locations of the Galileo X-line (magenta line) are located within the simulated bipolar $B_\theta$-dominated ranges, indicating the consistency of the reconnection positions between the quiet-time MHD simulations and the average satellite observations.

When the SW ram pressure is enhanced and the Jovian magnetosphere is significantly compressed (Figure 7b), the MLT coverage of the bipolar $B_\theta$-dominated ranges in the inner magnetotail is reduced from 21:00–5:30 MLT to 22:30–3:30 MLT. The boundary between $B_\theta$ positive and bipolar ranges near the inner magnetotail during SW compression periods is slightly more planetward by 0–10 $R_J$ near and after midnight (after 23:40 MLT), but significantly more tailward by 10–50 $R_J$ during pre-midnight (before 23:40 MLT) with respect to quiet-time condition (Figure 7a) and the average Galieo X-line (magenta line in Figure 7). This indicates that the SW compression does not significantly affect the radial distribution of the average reconnection position near and after midnight but suppresses reconnection during the pre-midnight. In general, the enhanced ram pressure can decrease the MLT coverage and induce a larger dawn-dusk asymmetry in the radial distribution of magnetotail reconnection.

In Figure 8, the inner magnetic field lines (blue lines) on the planetward side of the X-line are closed at both planets, but these lines extend from the north to south poles at Jupiter and display opposite directions at Earth. The plasmoid magnetic field lines (black lines) on the tailward side of the X-line exhibit turbulent and flux rope structures with multiple twists, indicating that these complex configurations are a consequence of multiple magnetotail reconnections at different times, rather than just a single isolated reconnection. These simulations reveal a significant difference between Jupiter and Earth. Specifically, at Earth, the plasmoid flux rope near the X-line has significant north-south symmetry, whereas the Jovian simulation lacks the ideal north-south symmetry in the magnetotail. This implies the equatorial $B_z$ zero lines, which are used to define the approximate locations of the X-line in this study and previous observations, may not correspond strictly to the X-line in the Jovian magnetotail. This discrepancy likely arises from the significant dynamic nature of the Jovian rotation-driven magnetotail. Additionally, different planetary rotation speeds at Jupiter and Earth also cause significant differences in lobe magnetic field lines near the X-line. Specifically, at Earth, the lobe magnetic field lines near the X-line through the midnight meridian are open, but in Jupiter, they

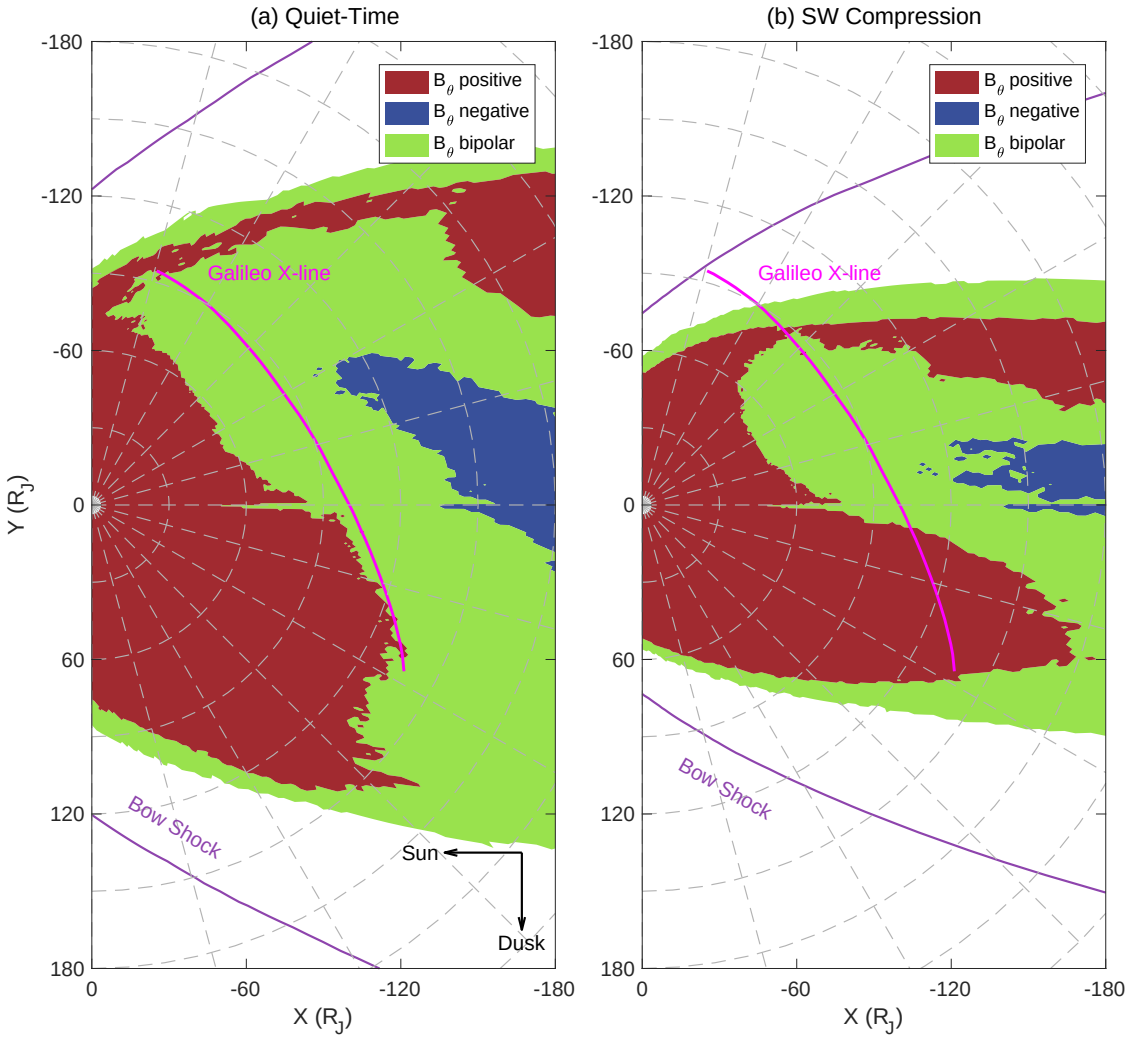


**Figure 7.** Distribution of the dominant $B_\theta$ signature in the MHD simulation during (a) quiet-time periods between 300:00–345:00 ST and (b) the later phase of SW compression between 360:00–390:00 ST. The colored ranges indicate the prevalence of different types of dominated signatures at the calculation grids. Red ranges signify where positive $B_\theta$ signatures are most common ($> 85\%$), blue ranges indicate where negative $B_\theta$ signatures are most common ($> 50\%$), and green ranges indicate where neither positive nor negative $B_\theta$ signatures are dominant. The magenta lines represent the Galileo X-line. This is an equatorial view with the sun positioned to the left.

exhibit a helical structure and are mostly closed, extending from the polar regions to the distant tail with east-west components. This unique feature is dominated by Jovian fast rotation, as demonstrated in the simulation work by Chen et al. (2023) and predicted by the theoretical frameworks by Hill (1979) and Isbell et al. (1984).

Although most features of the simulated Jovian magnetotail are consistent with satellite observations and theoretical predictions, other factors, such as dynamic changes in upstream SW conditions and the presence of hot plasma populations, may also have a significant impact. While the Jovian magnetosphere remains relatively stable (although still dynamic) during the quiet SW period and the later stages of SW compression (300:00–345:00 and 360:00–390:00 ST), Movie S1 displays largely unstable states during the early stages of SW compression at 345:00–360:00 ST. During this period, the magnetosphere experiences rapid compression by the enhanced SW ram pressure, similar to a pressed sponge. Energy and mass are also rapidly released into the far magnetotail. Besides the significantly dynamic response

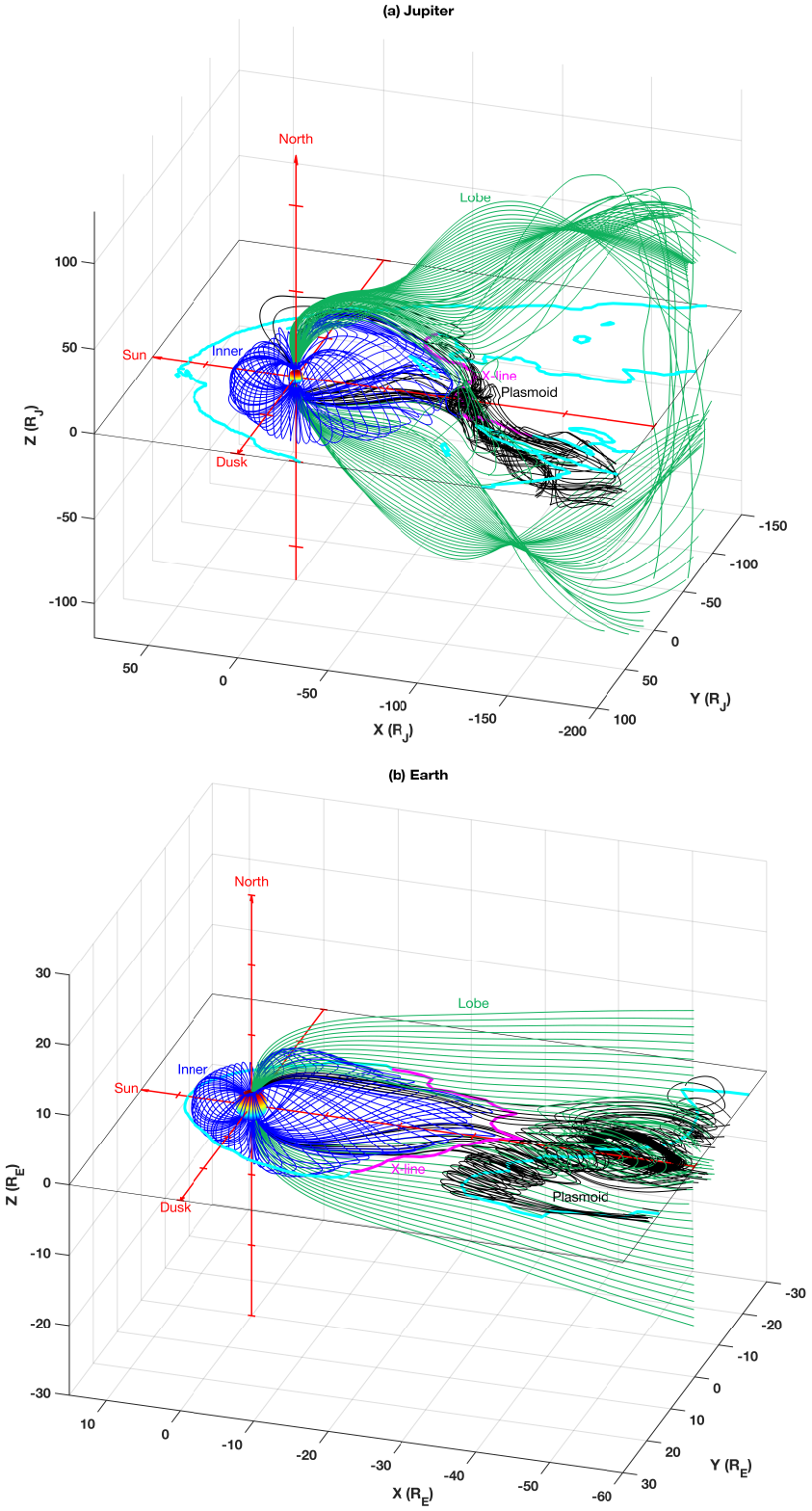


**Figure 8.** Comparison of magnetospheric magnetic field lines associated with magnetotail reconnection at Jupiter and Earth. Panel (a) depicts the Jovian results obtained from the MHD data with the eastward IMF at 300:00 ST, which is the same snapshot shown in Figures 3a and 4. Panel (b) shows the terrestrial results from the MHD data with southward IMF of $B_z$ = -10 nT and quiet SW density and velocity of 5 $cm^{-3}$ and 400 $km/s$ at 23:40 MLT, as used in (Zhang et al. 2020). The blue lines indicate the magnetic fields near the inner magnetosphere, while the green lines represent the lobe magnetic lines through the midnight meridian. The black lines denote the plasmoid magnetic fields passing through areas outside the locations of the X-line (magenta line). Additionally, the contours of $B_z = 0$ at the equatorial plane are represented by cyan lines. The colorful spheres represent the inner boundaries at Jovi-centric 3 $R_J$ in the Jovian run and at geocentric 2 Earth radii ($R_E$) in the terrestrial run.

in the Jovian magnetosphere, the field-aligned current and Alfvénic power in the inner magnetosphere or ionosphere also display complex responses (Feng et al. 2022). It is important to note that although this simulation study uses ideal upstream SW conditions, the Jovian magnetospheric responses are still highly dynamic. Therefore, it is expected that Jupiter's magnetosphere is even more complex under changing real SW conditions, though there is not enough upstream SW data available. On the other hand, the MHD simulation does not consider hot plasma populations, resulting in a slightly smaller Jovian magnetosphere (Figure 3) that may influence magnetotail reconnection, especially in the premidnight sector in Figures 6-7. Overall, further investigations are required to fully understand these two effects.

## 4. CONCLUSION

In this study, we utilized a three-dimensional global MHD model to simulate Jovian magnetotail reconnection and compared our results with observations from the Galileo and Juno spacecrafts. Our simulations generally reproduce the distribution and occurrence of magnetotail reconnection as observed by both spacecrafts. We discovered that magnetotail reconnection is more frequent in the midnight and post-midnight sectors, but less so in the pre-midnight sector. This is generally consistent with both Galileo and Juno observations and predictions by Delamere & Bagenal (2013) . Our simulations indicate that Jovian magnetotail reconnection is dynamic rather than steady-state, with a broad distribution in both MLT and radial distance. The enhanced SW ram pressure can decrease the MLT coverage of magnetotail reconnection by compressing the Jovian magnetosphere. Near the midnight and post-midnight sectors, the occurrence of magnetotail reconnection is enhanced by SW compression beyond 60 $R_J$ but is not significantly impacted by SW compression within 60 $R_J$. On the other hand, SW compression may suppress reconnection in the pre-midnight sector, leading to a stronger dawn-dusk asymmetry in the occurrence and location of magnetotail reconnection.

This work is supported by the Excellent Young Scientists Fund (Hong Kong and Macau) of the National Natural Science Foundation of China (Grant No. 41922060) and RGC General Research Fund (Grant No. 17308520 and 17315222). The model outputs used to generate the figures for analysis presented in this paper are being preserved online (https://doi.org/10.17605/OSF.IO/5M72X).

## APPENDIX

Figure 9 provides an example of $B_z$ reversal positions at 300:00 ST by the method mentioned in 2.2.

## REFERENCES

Ajello, J., Shemansky, D., Pryor, W., et al. 1998, Journal of Geophysical Research: Planets, 103, 20125, doi: 10.1029/98JE00832

Bagenal, F., & Delamere, P. A. 2011, Journal of Geophysical Research: Space Physics, 116, doi: 10.1029/2010JA016294

Biskamp, D. 1996, Astrophysics and Space Science, 242, 165, doi: 10.1007/BF00645113

Blanc, M., Kallenbach, R., & Erkaev, N. V. 2005, Space Science Reviews, 116, 227, doi: 10.1007/s11214-005-1958-y

Bonfond, B., Yao, Z., & Grodent, D. 2020, Journal of Geophysical Research: Space Physics, 125, e2020JA028152, doi: 10.1029/2020JA028152

Brambles, O. J., Lotko, W., Zhang, B., et al. 2011, Science, 332, 1183, doi: 10.1126/science.1202869

Chané, E., Saur, J., & Poedts, S. 2013, Journal of Geophysical Research: Space Physics, 118, 2157, doi: 10.1002/jgra.50258

Chen, J., Zhang, B., Lin, D., et al. 2023, Geophysical Research Letters, 50, e2022GL102577, doi: 10.1029/2022GL102577

Connerney, J. E. P., Adriani, A., Allegrini, F., et al. 2017, Science, 356, 826, doi: 10.1126/science.aam5928

Cowley, S. W. H., Badman, S. V., Imber, S. M., & Milan, S. E. 2008, Geophysical Research Letters, 35, doi: 10.1029/2007GL032645

Cowley, S. W. H., Bunce, E. J., Stallard, T. S., & Miller, S. 2003, Geophysical Research Letters, 30, doi: 10.1029/2002GL016030

Delamere, P. A., & Bagenal, F. 2010, Journal of Geophysical Research: Space Physics, 115, doi: 10.1029/2010JA015347

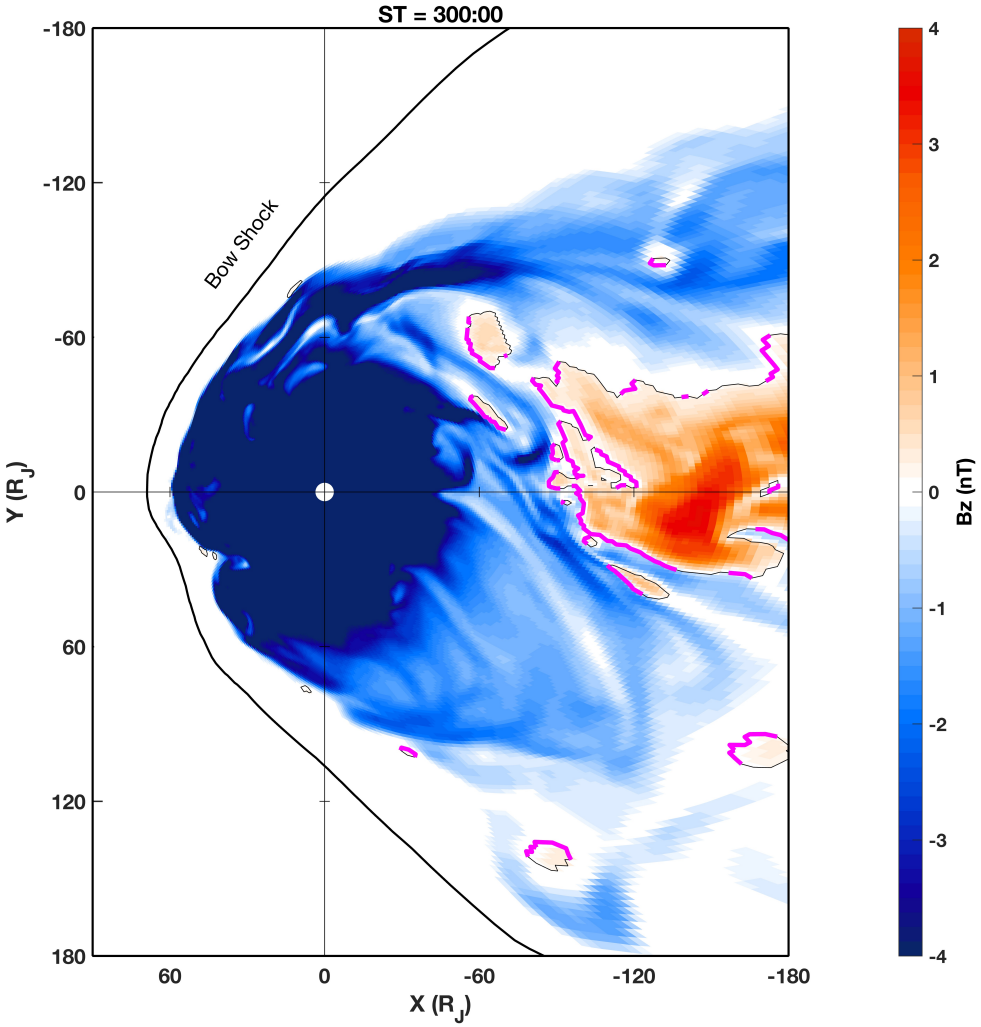


**Figure 9.** The distribution of the north-south component of the magnetic field ($B_z$, positive northward) at the equatorial plane of Jupiter's magnetosphere at 300:00 simulation time (ST) from the GAMERA. The magenta lines represent the $B_z$ reversal positions, where $B_z$ has a reversal from southward (parallel to the inner background field) to northward (antiparallel to the inner field) as radial distance increases at a given azimuthal angle on the nightside ($X < 0$).


—. 2013, Journal of Geophysical Research: Space Physics, 118, 7045, doi: 10.1002/2013JA019179

Delamere, P. A., Bagenal, F., Paranicas, C., et al. 2015, Space Science Reviews, 187, 51, doi: 10.1007/s11214-014-0075-1

Feng, E., Zhang, B., Yao, Z., et al. 2022, Geophysical Research Letters, 49, e2022GL099858, doi: 10.1029/2022GL099858

—. 2023, Geophysical Research Letters, 50, e2023GL104046, doi: 10.1029/2023GL104046

Frank, L. A., Paterson, W. R., & Khurana, K. K. 2002, Journal of Geophysical Research: Space Physics, 107, SIA 1, doi: 10.1029/2001JA000077

Fukazawa, K., Ogino, T., & Walker, R. J. 2006, Journal of Geophysical Research: Space Physics, 111, doi: 10.1029/2006JA011874

Ge, Y. S., Jian, L. K., & Russell, C. T. 2007, Geophysical Research Letters, 34, doi: 10.1029/2007GL031987

Gladstone, G. R., Persyn, S. C., Eterno, J. S., et al. 2017, Space Science Reviews, 213, 447, doi: 10.1007/s11214-014-0040-z

Grodent, D., Bonfond, B., Yao, Z., et al. 2018, Journal of Geophysical Research: Space Physics, 123, 3299, doi: https://doi.org/10.1002/2017JA025046

Gu, W. D., Yao, Z. H., Pan, D. X., et al. 2023, Journal of Geophysical Research: Planets, 128, e2022JE007625, doi: 10.1029/2022JE007625

Guo, R. L., Yao, Z. H., Grodent, D., et al. 2021, Geophysical Research Letters, 48, e2021GL093964, doi: https://doi.org/10.1029/2021GL093964

Gérard, J. C., Mura, A., Bonfond, B., et al. 2018, Icarus, 312, 145, doi: 10.1016/j.icarus.2018.04.020

Hanlon, P. G., Dougherty, M. K., Krupp, N., et al. 2004, Journal of Geophysical Research: Space Physics, 109, doi: 10.1029/2003JA010116

Hill, M. E., Haggerty, D. K., McNutt Jr, R. L., & Paranicas, C. P. 2009, Journal of Geophysical Research: Space Physics, 114, doi: 10.1029/2009JA014374

Hill, T. W. 1979, Journal of Geophysical Research: Space Physics, 84, 6554, doi: 10.1029/JA084iA11p06554

Huscher, E., Bagenal, F., Wilson, R. J., et al. 2021, Journal of Geophysical Research: Space Physics, 126, e2021JA029446, doi: 10.1029/2021JA029446

Isbell, J., Dessler, A. J., & Waite Jr, J. H. 1984, Journal of Geophysical Research: Space Physics, 89, 10716, doi: 10.1029/JA089iA12p10716

Jackman, C. M., & Arridge, C. S. 2011, Solar Physics, 274, 481, doi: 10.1007/s11207-011-9748-z

Jackman, C. M., Arridge, C. S., Slavin, J. A., et al. 2010, Journal of Geophysical Research: Space Physics, 115, doi: 10.1029/2010JA015312

Jia, X., Hansen, K. C., Gombosi, T. I., et al. 2012, Journal of Geophysical Research: Space Physics, 117, doi: 10.1029/2012JA017575

Kasahara, S., Kronberg, E. A., Kimura, T., et al. 2013, Journal of Geophysical Research: Space Physics, 118, 375, doi: 10.1029/2012JA018130

Khurana, K. K., Kivelson, M. G., Vasyliunas, V. M., et al. 2004, The configuration of Jupiter's magnetosphere, Vol. 1 (Cambridge Univ. Press Cambridge, U. K), 593–616. https://ui.adsabs.harvard.edu/abs/2004jpsm.book..593K

Kronberg, E. A., Woch, J., Krupp, N., et al. 2005, Journal of Geophysical Research: Space Physics, 110, doi: 10.1029/2004JA010777

Kurth, W. S., Sullivan, J. D., Gurnett, D. A., et al. 1982, Journal of Geophysical Research: Space Physics, 87, 10373, doi: 10.1029/JA087iA12p10373

Lyon, J. G., Fedder, J. A., & Mobarry, C. M. 2004, Journal of Atmospheric and Solar-Terrestrial Physics, 66, 1333, doi: 10.1016/j.jastp.2004.03.020

Masters, A. 2018, Geophysical Research Letters, 45, 7320, doi: 10.1029/2018GL078416

Mauk, B. H., Clarke, J. T., Grodent, D., et al. 2002, Nature, 415, 1003, doi: 10.1038/4151003a

McComas, D. J., & Bagenal, F. 2007, Geophysical Research Letters, 34, doi: 10.1029/2007GL031078

—. 2008, Geophysical Research Letters, 35, doi: 10.1029/2008GL034351

McNutt, R. L., Haggerty, D. K., Hill, M. E., et al. 2007, Science, 318, 220, doi: 10.1126/science.1148025

Miyoshi, T., & Kusano, K. 2001, Journal of Geophysical Research: Space Physics, 106, 10723, doi: 10.1029/2000JA900153

Moriguchi, T., Nakamizo, A., Tanaka, T., Obara, T., & Shimazu, H. 2008, Journal of Geophysical Research: Space Physics, 113, doi: 10.1029/2007JA012751

Nichols, J. D., Bunce, E. J., Clarke, J. T., et al. 2007, Journal of Geophysical Research: Space Physics, 112, doi: 10.1029/2006JA012005

Nichols, J. D., Kamran, A., & Milan, S. E. 2019, Journal of Geophysical Research: Space Physics, 124, 8884, doi: 10.1029/2019JA027120

Nishida, A. 1983, Geophysical Research Letters, 10, 451, doi: 10.1029/GL010i006p00451

Ogino, T., Walker, R. J., & Kivelson, M. G. 1998, Journal of Geophysical Research: Space Physics, 103, 225, doi: 10.1029/97JA02247

Ouellette, J. E., Brambles, O. J., Lyon, J. G., Lotko, W., & Rogers, B. N. 2013, Journal of Geophysical Research: Space Physics, 118, 3223, doi: 10.1002/jgra.50309

Parker, E. 1979, The International Series of Monographs on Physics

Priest, E., & Forbes, T. 2000, Magnetic Reconnection: MHD Theory and Applications (Cambridge: Cambridge University Press), doi: 10.1017/CBO9780511525087

Russell, C. T., Khurana, K. K., Huddleston, D. E., & Kivelson, M. G. 1998, Science, 280, 1061, doi: 10.1126/science.280.5366.1061

Sarkango, Y., Jia, X., & Toth, G. 2019, Journal of Geophysical Research: Space Physics, 124, 5317, doi: 10.1029/2019JA026787

Schok, A. A., Delamere, P. A., Mino, B., et al. 2023, Journal of Geophysical Research: Planets, 128, e2022JE007637, doi: 10.1029/2022JE007637

Smith, E. J., Fillius, R. W., & Wolfe, J. H. 1978, Journal of Geophysical Research: Space Physics, 83, 4733, doi: 10.1029/JA083iA10p04733

Song, P., DeZeeuw, D. L., Gombosi, T. I., Kozyra, J. U., & Powell, K. G. 2001, Advances in Space Research, 28, 1763, doi: 10.1016/S0273-1177(01)00544-0

Szego, K., Achilleos, N., Arridge, C., et al. 2016, The Magnetodiscs and Aurorae of Giant Planets (Springer)

Tanaka, T., Ebihara, Y., Watanabe, M., Fujita, S., & Kataoka, R. 2021, Journal of Geophysical Research: Space Physics, 126, e2021JA029232, doi: 10.1029/2021JA029232

Tao, C., Kataoka, R., Fukunishi, H., Takahashi, Y., & Yokoyama, T. 2005, Journal of Geophysical Research: Space Physics, 110, doi: 10.1029/2004JA010959

Thomas, N., Bagenal, F., Hill, T., et al. 2004, F. Bagenal, T. Dowling, WB McKinnon, Eds, 561, 561

Vasyliunas, V. M. 1983, Physics of the Jovian magnetosphere, 395

Vogt, M. F., Gyalay, S., Kronberg, E. A., et al. 2019, Journal of Geophysical Research: Space Physics, 124, 10170, doi: 10.1029/2019JA026950

Vogt, M. F., Jackman, C. M., Slavin, J. A., et al. 2014, Journal of Geophysical Research: Space Physics, 119, 821, doi: 10.1002/2013JA019393

Vogt, M. F., Kivelson, M. G., Khurana, K. K., Joy, S. P., & Walker, R. J. 2010, Journal of Geophysical Research: Space Physics, 115, doi: 10.1029/2009JA015098

Vogt, M. F., Connerney, J. E. P., DiBraccio, G. A., et al. 2020, Journal of Geophysical Research: Space Physics, 125, e2019JA027486, doi: 10.1029/2019JA027486

Waite, J. H., Bagenal, F., Seward, F., et al. 1994, Journal of Geophysical Research: Space Physics, 99, 14799, doi: 10.1029/94JA01005

Waite, J. H., Gladstone, G. R., Lewis, W. S., et al. 2001, Nature, 410, 787, doi: 10.1038/35071018

Wang, Y., Guo, X., Tang, B., Li, W., & Wang, C. 2018, Earth and Planetary Physics, 2, 303, doi: 10.26464/epp2018028

Wang, Y., Yang, J., Guo, X., Wang, C., & Blanc, M. 2023, Journal of Geophysical Research: Space Physics, 128, e2022JA031132, doi: 10.1029/2022JA031132

Woch, J., Krupp, N., & Lagg, A. 2002, Geophysical Research Letters, 29, 42, doi: 10.1029/2001GL014080

Yamada, M., Kulsrud, R., & Ji, H. 2010, Reviews of Modern Physics, 82, 603, doi: 10.1103/RevModPhys.82.603

Yang, J., Wolf, R., Toffoletto, F., et al. 2019, Journal of Geophysical Research: Space Physics, 124, 10294, doi: 10.1029/2019JA026811

Yao, Z. H., Bonfond, B., Clark, G., et al. 2020, Journal of Geophysical Research: Space Physics, 125, e2019JA027663, doi: 10.1029/2019JA027663

Yao, Z. H., Bonfond, B., Grodent, D., et al. 2022, Journal of Geophysical Research: Space Physics, 127, e2021JA029894, doi: 10.1029/2021JA029894

Zhang, B., Brambles, O. J., Cassak, P. A., et al. 2017, Journal of Geophysical Research: Space Physics, 122, 9474, doi: 10.1002/2016JA023646

Zhang, B., Brambles, O. J., Lotko, W., & Lyon, J. G. 2020, Geophysical Research Letters, 47, e2019GL086419, doi: 10.1029/2019GL086419

Zhang, B., Brambles, O. J., Wiltberger, M., et al. 2016, Geophysical Research Letters, 43, 1837, doi: 10.1002/2016GL068005

Zhang, B., Delamere, P. A., Ma, X., et al. 2018, Geophysical Research Letters, 45, 56, doi: 10.1002/2017gl076315

Zhang, B., Sorathia, K. A., Lyon, J. G., et al. 2019, The Astrophysical Journal Supplement Series, 244, 20, doi: 10.3847/1538-4365/ab3a4c

Zhang, B., Delamere, P. A., Yao, Z., et al. 2021, Science Advances, 7, eabd1204, doi: 10.1126/sciadv.abd1204